

1 High-order dynamic neural correlations reflect naturalistic 2 processing in humans

Lucy L. W. Owen¹, Thomas H. Chang^{1,2}, and Jeremy R. Manning^{1,†}

¹Department of Psychological and Brain Sciences,
Dartmouth College, Hanover, NH

³Amazon.com, Seattle, WA

[†]Address correspondence to jeremy.r.manning@dartmouth.edu

July 29, 2019

Abstract

Our thoughts arise from coordinated activity patterns across our brain. We examined high-order dynamic correlations in functional neuroimaging data collected as human participants listened to different auditory stimuli varying in cognitive richness, along with an additional resting state condition. Our approach combines a kernel-based method for estimating the dynamic functional correlations that are similar (within task) across participants, along with a dimensionality reduction approach that enables us to efficiently compute high-order correlations in the data. We trained classifiers to decode the precise time, relative to the start of the stimulus, when a given neural pattern was recorded. We trained these classifiers using the neural activity timeseries, first-order dynamic correlations, and higher-order correlations (up to tenth-order correlations), and asked which types of features led to the highest decoding accuracy. We found that higher-order correlations consistently yielded higher decoding accuracy for the most cognitively rich condition of the experiment, whereas first-order correlations or raw data yielded the highest decoding accuracy at for the less cognitively rich conditions as well as rest.

¹⁸ Introduction

19 To understand the neuronal computations that support cognition, we must understand the cooperative
20 dynamics of populations of neurons. These populations of neurons interact within each brain structure,
21 and the structures interact to form complex and dynamic networks. These interactions, at each scale, vary
22 according to the functions our brains are carrying out.

In the last several decades, advances in functional magnetic resonance image (fMRI) analyses have evolved to better characterize these interactions of brain structures. As Turk-Brown (2013) outlines, analyses using multivariate patterns of activity have given an advance over univariate activity patterns because they allow relative contributions of voxels to be combined and better assess distributed representations. Resting-state connectivity (RS) fMRI, which is the temporal correlation of regions during rest, has shed light on the rich and complex spatiotemporal organization of spontaneous brain activity. Functional connectivity (FC) has further characterized the cognitive state dependency of this network organization.

30 Recent work has shown that FC fluctuates over time (Chang and Glover, 2010), and the assumed
31 stationarity of these analyses may be too simple to capture the dynamic nature of brain activity. Additionally,
32 recent work show that dynamic correlations between multivariate voxel patterns can add an additional boost
33 (Manning, 2018). Following this line of reasoning, we expect higher-order network dynamics might provide
34 even richer insights into the neural basis of cognition. We sought to test this hypothesis by developing an
35 approach to inferring high-order network dynamics from timeseries data, validating the approach using
36 synthetic data, and then applying the approach to a neuroimaging dataset comprising data collected as
37 participants listened to a story (Simony et al., 2016). We tested the hypothesis that as people listen to stimuli
38 varying in cognitive richness, the neural patterns that support processing of those stimuli vary with respect
39 to the order of the dynamic interactions recruited.

40 **Methods**

41 A major challenge to studying such patterns is that typically neither the correlations nor the hierarchical
42 organizations of those correlations may be directly observed. Rather, these fundamental properties must
43 be inferred indirectly by examining the observable parts of the system—e.g., the behaviors of the individual
44 units of that system. Here we propose a series of mathematical operations that may be used to approximate
45 dynamic correlations at a range of scales (i.e., orders of interaction).

46 There are two basic steps to our approach (Fig. 2). In the first step, we take a number-of-timepoints (T)
47 by number-of-features (F) *matrix of observations* (\mathbf{X}) and we return a T by $\frac{F^2-F}{2}$ *matrix of dynamic correlations*
48 (\mathbf{Y}). Here \mathbf{Y}_0 describes, at each moment, how all of the features (columns of \mathbf{X}) are inferred to be interacting.
49 (Since the interactions are assumed to be non-recurrent and symmetric, only the upper triangle of the full
50 correlation matrix is computed.) In the second step, we project \mathbf{Y}_0 onto an F -dimensional space, resulting in
51 a new T by F matrix \mathbf{Y}_1 . Note that \mathbf{Y}_1 contains information about the correlation dynamics present in \mathbf{X} , but
52 represented in a compressed number of dimensions. By repeatedly applying these two steps in sequence,
53 we can examine and explore higher order dynamic correlations in \mathbf{X} .

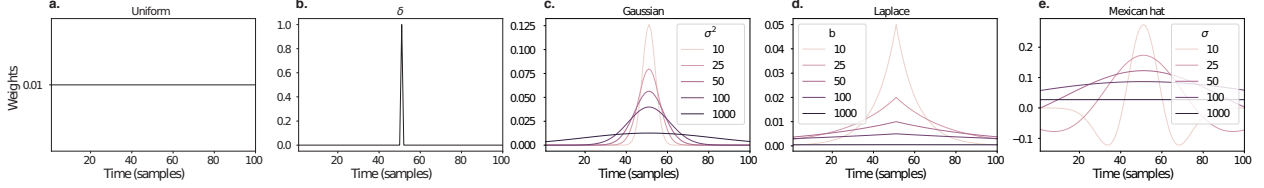


Figure 1: **Examples of time-varying weights.** Each panel displays per-timepoint weights at $t = 50$, evaluated for 100 timepoints (1, ..., 100). **a. Uniform weights.** The weights are timepoint-invariant; observations at all timepoints are weighted equally, and do not change as a function of t . This is a special case of weight function that reduces dynamic correlations to static correlations. **b. Dirac delta function.** Only the observation at timepoint t is given weight (of 1), and weights for observations at all other timepoints are set to 0. **c. Gaussian weights.** Each observation's weights fall off in time according to a Gaussian probability density function centered on $\mu = t$. Weights derived using several different example variance parameters (σ^2) are displayed. **d. Laplace weights.** Each observation's weights fall off in time according to a Laplace probability density function centered on $\mu = t$. Weights derived using several different example scale parameters (b) are displayed. **e. Mexican hat (Ricker wavelet) weights.** Each observation's weights fall off in time according to a Ricker wavelet centered on t . This function highlights the *contrasts* between local versus surrounding activity patterns in estimating dynamic correlations. Weights derived using several different example width parameters (σ) are displayed.

54 Dynamic correlations

Given a matrix of observations, we can compute the (static) correlations between any pair of observations, \mathbf{X}_i and \mathbf{X}_j using:

$$\text{corr}(\mathbf{X}_i, \mathbf{X}_j) = \frac{\sum_{t=1}^T (\mathbf{X}_i(t) - \bar{\mathbf{X}}_i)(\mathbf{X}_j(t) - \bar{\mathbf{X}}_j)}{\sqrt{\sum_{t=1}^T \sigma_{\mathbf{X}_i}^2 \sigma_{\mathbf{X}_j}^2}}, \text{ where} \quad (1)$$

$$\bar{\mathbf{X}}_k = \sum_{t=1}^T \mathbf{X}_k(t), \text{ and} \quad (2)$$

$$\sigma_{\mathbf{X}_k}^2 = \sum_{t=1}^T (\mathbf{X}_k(t) - \bar{\mathbf{X}}_k)^2 \quad (3)$$

55 We can generalize this formula to compute time-varying correlations by incorporating a *weight function*
 56 that takes a time t as input, and returns how much the observed data every timepoint (including t) contribute
 57 to the correlations at time t (Fig. 1).

Given a weight function $w(t)$ for timepoint t , evaluated at timepoints in the interval $[1, \dots, T]$, we can

extend the static correlation formula in Equation 2 to reflect an *instantaneous correlation* at timepoint t :

$$\text{timecorr}(\mathbf{X}_i, \mathbf{X}_j, t) = \frac{\sum_{t=1}^T (\mathbf{X}_i(t) - \tilde{\mathbf{X}}_i(t))(\mathbf{X}_j(t) - \tilde{\mathbf{X}}_j(t))}{\sqrt{\sum_{t=1}^T \tilde{\sigma}_{\mathbf{X}_i}^2(t) \tilde{\sigma}_{\mathbf{X}_j}^2(t)}}, \text{ where} \quad (4)$$

$$\tilde{\mathbf{X}}_k(t) = \sum_{i=1}^T w(t, i) \mathbf{X}_k(i), \quad (5)$$

$$\tilde{\sigma}_{\mathbf{X}_k}^2(t) = \sum_{i=1}^T (\mathbf{X}_k(i) - \tilde{\mathbf{X}}_k(t))^2, \quad (6)$$

and $w(t, i)$ is shorthand for $w(t)$ evaluated at timepoint i . Equation 5 may be used to estimate the instantaneous correlations between every pair of observations, at each timepoint (i.e., \mathbf{Y}).

60 Inter-subject dynamic correlations

Equation 5 provides a means of taking a single observation matrix, \mathbf{X} and estimating the dynamic correlations from moment to moment, \mathbf{Y} . Suppose that one has access to a set of multiple observation matrices that reflect the same phenomenon. For example, one might collect neuroimaging data from several experimental participants, as each participant performs the same task (or sequence of tasks). Let $\mathbf{X}_1, \mathbf{X}_2, \dots, \mathbf{X}_P$ reflect the T by F observation matrices for each of P participants in an experiment. We can use *inter-subject functional connectivity* (ISFC; Simony et al., 2016) to compute the degree of stimulus-driven correlations reflected in the multi-participant dataset at a given timepoint t using:

$$\bar{\mathbf{C}}(t) = M \left(R \left(\frac{1}{2P} \sum_{i=1}^P Z(Y_i(t))^T + Z(Y_i(t)) \right) \right), \quad (7)$$

where M extracts and vectorizes the diagonal and upper triangle of a symmetric matrix, Z is the Fisher z-transformation (Zar, 2010):

$$Z(r) = \frac{\log(1+r) - \log(1-r)}{2} \quad (8)$$

R is the inverse of Z :

$$R(z) = \frac{\exp(2z-1)}{\exp(2z+1)}, \quad (9)$$

and $\mathbf{Y}_i(t)$ denotes the correlation matrix (Eqn. 2) between each column of \mathbf{X}_i and each column of the average observations from all *other* participants, $\bar{\mathbf{X}}_{\setminus i}$:

$$\bar{\mathbf{X}}_{\setminus i} = R \left(\frac{1}{P-1} \sum_{i \in \setminus i} Z(\mathbf{X}_i) \right), \quad (10)$$

61 where $\setminus i$ denotes the set of all participants other than participant i . In this way, the T by $\left(\frac{F^2-F}{2} + F\right)$ matrix $\bar{\mathbf{C}}$
62 is the time-varying extension of the ISFC approach developed by Simony et al. (2016).

63 Higher-order correlations

64 Given a timeseries of dynamic correlations (e.g., obtained using Eqn. 5), higher-order correlations reflect the
65 dynamic correlations between columns of \mathbf{Y} . Given unlimited computing resources, one could use repeated
66 applications of Equation 5 to estimate these higher-order correlations (i.e., substituting in the previous
67 output, \mathbf{Y} , for the input, \mathbf{X} in the equation). However, because each output \mathbf{Y} has $O(F^2)$ columns relative
68 to F columns in the input \mathbf{X} , the output of Equation 5 grows with the square of the number of repeated
69 applications (total cost of computing n^{th} order correlations is $O(F^{2n})$ for $n \in \mathcal{J}, n > 0$). When F or n is large,
70 this approach quickly becomes intractable.

71 To make progress in computing \mathbf{Y}_{n+1} , we can approximate \mathbf{Y}_n by computing an $O(F)$ -dimensional em-
72 bedding of \mathbf{Y}_n , termed $\hat{\mathbf{Y}}_n$, and then we can apply Equation 5 to $\hat{\mathbf{Y}}_n$ rather than directly to \mathbf{Y}_n . This enables
73 us to maintain $O(n)$ scaling with respect to n , rather than exponential scaling via the direct approach.

74 There are many possible methods for computing $\hat{\mathbf{Y}}_n$ from \mathbf{Y}_n , including traditional dimensionality
75 reduction approaches and graph theory based approaches as described next. In the *Discussion* section we
76 elaborate on other potential approaches.

77 Dimensionality reduction-based approaches to computing $\hat{\mathbf{Y}}_n$

78 Commonly used dimensionality reduction algorithms include Principal Components Analysis (PCA; Pear-
79 son, 1901), Probabilistic PCA (PPCA; Tipping & Bishop, 1999), Exploratory Factor Analysis (EFA; Spearman,
80 1904), Independent Components Analysis (ICA; Jutten & Herault, 1991; Comon et al., 1991), t -Stochastic
81 Neighbor Embedding (t -SNE; van der Maaten & Hinton, 2008), Uniform Manifold Approximation and
82 Projection (UMAP; McInnes & Healy, 2018), non-negative matrix factorization (NMF; Lee & Seung,
83 1999), Topographic Factor Analysis (TFA) Manning et al. (2014), Hierarchical Topographic Factor analysis
84 (HTFA) Manning et al. (2018), Topographic Latent Source Analysis (TLSA) Gershman et al. (2011), Dictio-
85 nary learning (J. B. Mairal et al., 2009; J. Mairal et al., 2009), deep autoencoders (Hinton & Salakhutdinov,

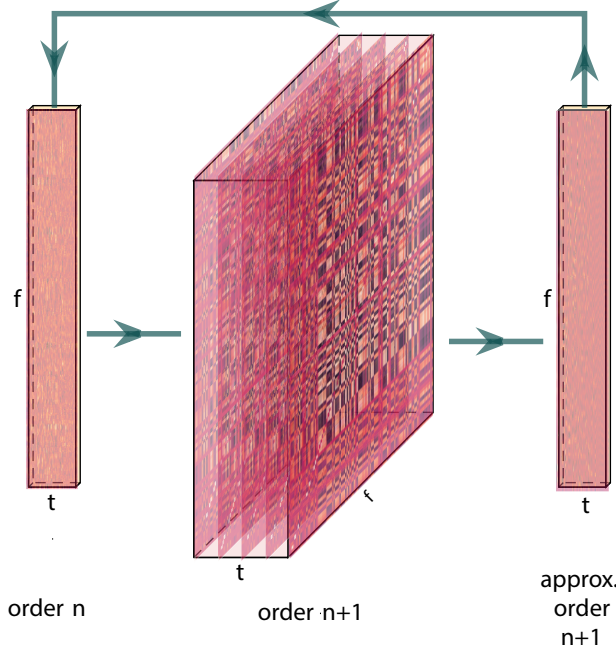


Figure 2: Computing higher order correlations. Dynamic correlations are computed then approximated to the same size as original data using dimensionality reduction. This process is repeated, and can be used to compute up to any arbitrary order with computations scaling linearly (as opposed to exponentially) with order.

86 2006), among others. While complete characterizations of each of these algorithms is beyond the scope of
 87 the present manuscript, the general intuition driving these approaches is to compute the $\hat{\mathbf{Y}}$ with i columns
 88 that is closest to the original \mathbf{Y} with j columns, and where (typically) $i \ll j$. The different approaches place
 89 different constraints on what properties $\hat{\mathbf{Y}}$ must satisfy and which aspects of the data are compared (and
 90 how) to characterize the match between $\hat{\mathbf{Y}}$ and \mathbf{Y} .

91 Applying dimensionality reduction algorithms to \mathbf{Y} yields a $\hat{\mathbf{Y}}$ whose columns reflect weighted combi-
 92 nations (or nonlinear transformations) of the original columns of \mathbf{Y} . This has two main consequences. First,
 93 with each repeated dimensionality reduction, the resulting $\hat{\mathbf{Y}}_n$ has lower and lower fidelity (with respect to
 94 what the “true” \mathbf{Y}_n might have looked like without using dimensionality reduction to maintain scalability).
 95 In other words, computing $\hat{\mathbf{Y}}_n$ is a lossy operation. Second, whereas the columns of \mathbf{Y}_n may be mapped
 96 directly onto pairs of columns of \mathbf{Y}_{n-1} , that mapping either becomes less cleanly defined in $\hat{\mathbf{Y}}_n$ due to the
 97 reweightings and/or nonlinear transformations.

98 **Graph theory-based approaches to computing $\hat{\mathbf{Y}}_n$**

99 Graph theoretic measures take as input a matrix of interactions (e.g., using the above notation, an $F \times F$
 100 correlation matrix or binarized correlation matrix reconstituted from a single timepoint’s row of \mathbf{Y}) and

101 return as output a set of F measures describing how each node (feature) sits within that interactions matrix
102 with respect to the rest of the population. Common measures include betweenness centrality (the proportion
103 of shortest paths between each pair of nodes in the population that involves the given node in question; e.g.,
104 Newman, 2005; Opsahl et al., 2010; Barthélemy, 2004; Geisberger et al., 2008; Freeman, 1977); diversity and
105 dissimilarity (characterizations of how differently connected a given node is from others in the population;
106 e.g., Rao, 1982; Lin, 2009; Ricotta & Szeidl, 2006); Eigenvector centrality and pagerank centrality (measures of
107 how influential a given node is within the broader network; e.g., Newman, 2008; Bonacich, 2007; Lohmann
108 et al., 2010; Halu et al., 2013); transfer entropy and flow coefficients (a measure of how much information is
109 flowing from a given node to other nodes in the network; e.g., Honey et al., 2007; Schreiber, 2000); k -coreness
110 centrality (a measure of the connectivity of a node within its local sub-graph; e.g., Alvarez-Hamelin et al.,
111 2005; Christakis & Fowler, 2010); within-module degree (a measure of how many connections a node has to
112 its close neighbors in the network; e.g., Rubinov & Sporns, 2010); participation coefficient (a measure of the
113 diversity of a node's connections to different sub-graphs in the network; e.g., Rubinov & Sporns, 2010); and
114 sub-graph centrality (a measure of a node's participation in all of the network's sub-graphs; e.g., Estrada &
115 Rodríguez-Velázquez, 2005).

116 As an alternative to the above dimensionality reduction approach to embedding \mathbf{Y}_n in a lower-dimensional
117 space, but still allowing for scalable explorations of higher-order structure in the data, we also explore using
118 the above graph theoretic measures as a means of obtaining $\hat{\mathbf{Y}}_n$. In particular: for a given graph theoretic
119 measure, $\eta : \mathcal{R}^{F \times F} \rightarrow \mathcal{R}^F$, we can use η to transform each row of \mathbf{Y}_n in a way that characterizes the cor-
120 responding graph-theoretic properties of each column. Whereas the dimensionality reduction approach
121 to computing $\hat{\mathbf{Y}}_n$ is lossy, the graph-theory approach is lossless. However, whereas the dimensionality
122 reduction approach maintains ties (direct or indirect) to the original activity patterns reflected in \mathbf{Y}_{n-1} , the
123 graph-theory approach does not. Instead, the graph-theory characterizes the nature and timecourse of each
124 feature's *participation* in the network.

125 Evaluation metrics

126 We evaluate our approach to extracting dynamic correlations and higher-order correlations using several
127 metrics detailed next. First, we generated synthetic data using known time-varying correlations, and then
128 we evaluated the fidelity with which Equation 5 could recover those correlations (for synthetic datasets
129 with different properties, and using different kernels to define the weights; Fig. 1). We then turned to a
130 series of analyses on a (real) neuroimaging dataset where the ground truth correlations were *not* known.
131 We evaluated whether the recovered correlations could be used to accurately label held-out neuroimaging

132 data with the time at which it was collected. We used this latter evaluations (using timepoint decoding)
133 as a proxy for gauging how much explanatory power the recovered correlations held with respect to the
134 observed data.

135 **Generating synthetic data**

136 To explore recovery of a constant covariance (Fig. 3, A.), we generated synthetic data sampled from a constant
137 covariance matrix. To do this, we created one random covariance matrix, K , with 50 features, and for each
138 of the 300 timepoints we sampled from a Gaussian distribution centered on K . Similarly, we generated
139 synthetic data sampled from a random covariance matrix (Fig. 3, B.) by creating a new random covariance
140 matrix $K(t)$, for each of the 300 timepoints and sampled from a Gaussian distribution centered on $K(t)$.

To generate synthetic data from a dynamically changing covariance matrix (Fig. 3, C.), we generated
two random covariance matrices, K_1 and K_2 . We then computed a weighted average covariance matrix for
each of the 300 timepoint, $K(t)$, by taking the linearly spaced weights (w) of the two random matrices,

$$K(t) = w(t) * K_1 + (1 - w(t)) * K_2, \quad (11)$$

$$(12)$$

141 and for each of the 300 timepoints sampled from a Gaussian distribution centered on $K(t)$.

142 Lastly, for the synthetic data containing block structure (Fig. 3, D.), we followed the same process of
143 creating synthetic data sampled from a constant covariance matrix (see above) but sampled from a new
144 random covariance matrix after 60 consecutive timepoints. We then pieced the blocks together to create a
145 synthetic dataset with 300 total timepoints but drawn from 5 separate covariance matrices.

146 **Recovery of ground truth parameters from synthetic data**

147 We applied timecorr, using delta and gaussian (width = 10) kernels Fig. 1 to each of these synthetic datasets,
148 then correlated each recovered correlation matrix with the ground truth. We repeated this process 10 times
149 and explored how recovery varies with the kernel and the specific structure of the data. For the ramping
150 synthetic dataset (Fig. 3, C.) and for the block synthetic dataset (Fig. 3, D.) we made further comparisons
151 of the timecorr recovered correlation matrices. We compared the ramping recovered correlation matrices to
152 only the first random covariance matrix K_1 (First, Fig. 3, C.) and to only the last random covariance matrix
153 K_2 (Last, Fig. 3, C.) from Equation 12. We also compared the block recovered correlation matrices in to the
154 block specific covariance matrix (Block 1-5, Fig. 3, D.).

155 **Timepoint decoding**

156 To explore how higher-order structure varies with stimulus structure and complexity, we used a previous
157 neuroimaging dataset Simony et al. (2016) in which participants listened to an audio recording of a story;
158 36 participants listen to an intact version of the story, 17 participants listen to time-scrambled recordings of
159 the same story where paragraphs were scrambled, 36 participants listen to word-scrambled version and 36
160 participants lay in rest condition.

161 Prior work has shown participants share similar neural responses to richly structured stimuli when
162 compared to stimuli with less structure. To assess whether the moment-by-moment higher order correlations
163 were reliably preserved across participants, we used inter-subject functional connectivity (ISFC) to isolate
164 the time-varying correlational structure (functional connectivity patterns that were specifically driven by
165 the story participants listened to. Following the analyses conducted by (HTFA) Manning et al. (2018), we
166 first applied *hierarchical topographic factor analysis* (HTFA) to the fMRI datasets to obtain a time series of
167 700 node activities for every participant. We then computed the dynamic weighted ISFC using a range of
168 kernels and widths. Specifically, we used Gaussian, Laplace, and mexican hat kernels, as well as widths of
169 5, 10, 20, and 50. We then approximated these dynamic correlation using two reduction measures, PCA and
170 eigenvector centrality, and computed the dynamic weighted ISFC on the approximations. We repeated this
171 process up to 10th order approximated correlations.

172 To assess decoding accuracy, we randomly divided participants for each stimulus into training and
173 testing groups. For the zeroth order, we computed the mean factor activity for each group. For all subsequent
174 orders up to the tenth order, we computed the mean approximated dynamic ISFC of factor activity for each
175 group. To assess how additional higher-order correlations contribute to decoding accuracy, for each order
176 we included a weighted-mixture (described below) of the activity patterns of all previous orders. For each
177 group of participants in turn, we compared these activity patterns (using Pearson correlations) to estimate
178 the story times each pattern corresponded to. Specifically, we asked, for each timepoint: what are the
179 correlations between the first group's and second group's activity patterns at each order. We note that the
180 decoding test we used is a conservative in which we count a timepoint label as incorrect if it is not an exact
181 match.

182 For each order we obtained the weighted-mixture of the correlation matrices for the current order and
183 all previous orders using mixing parameter , ϕ , where $0 < \phi < 1$ reflects a weighted mixture of order
184 based decoding Fig. 4 Panel C.). We calculated ϕ , by subdividing the training group and using the quasi-
185 Newton method of Broyden, Fletcher, Goldfarb, and Shanno (BFGS) for optimization. We repeated this
186 cross-validation process 100 times.

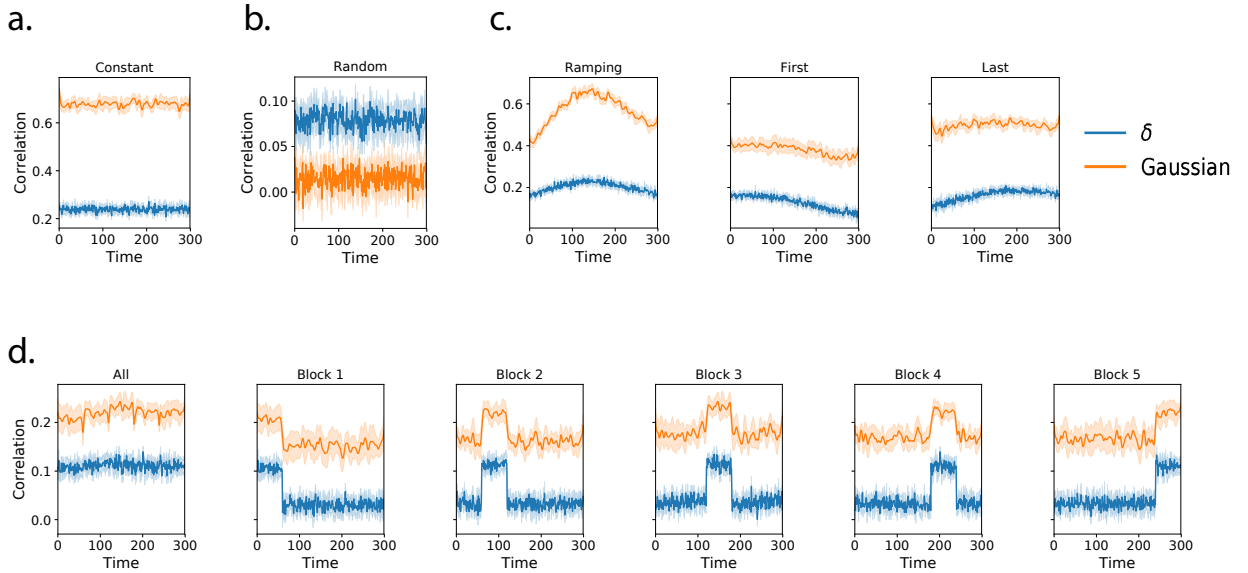


Figure 3: **Dynamic correlation recovery with synthetic data.** Using synthetic data containing different underlying correlational structure, we test how well we can recover dynamic correlation matrices using two kernels (delta and gaussian, width = 10) when compared to ground truth. We plot recovery using of datasets containing the following underlying structure: **a. Constant.** **b. Random.** **c. Ramping.** **d. Block.**

187 Results

188 Synthetic data

189 To assess the performance of dynamic correlation recovery using timecorr, we varied width the kernel and
 190 the specific structure of the data. We applied timecorr, using delta and gaussian kernels Fig. 1) to each of
 191 the following synthetic datasets: constant, random, ramping, and block. We then correlated each recovered
 192 correlation matrix with the ground truth.

193 For the constant synthetic dataset, a gaussian kernel (width=10) outperformed the delta kernel (Fig. 3,
 194 A.). This is in contrast with the random synthetic dataset, for which the delta kernel best captures the rapidly
 195 changing structure (Fig. 3, B.). For the ramping synthetic dataset, the slow changing strucutre within the
 196 data is best captured by the gaussian kernel and the best recovery occurs in the middle (Ramping, Fig. 3,
 197 C.). In addition to comparing the timecorr recovered correlation matrices to the ground truth, we further
 198 compared the ramping recovered correlation matrices to only the first random covariance matrix K_1 (First,
 199 Fig. 3, C.) and to only the last random covariance matrix K_2 (Last, Fig. 3, C.), both of which perform best at
 200 the beginning and end respectively.

201 Similary for the block sythetic dataset, we compared the timecorr recovered correlation matrices to
 202 the ground truth as well as to each block-specific covariance matrix (Block 1-5, Fig. 3, D.). Although the

203 structure is changing by block, the gaussian kernel once again outperforms the delta kernel. Performance
204 does however drop near even boundaries for when using the gaussian kernel.

205 **Neuroimaging dataset (Simony et al., 2016)**

206 For our decoding analysis, we used HTFA-derived node activities Manning et al. (2018) from fMRI data
207 collected as participants listened to an audio recording of a story (intact condition; 36 participants), lis-
208 tened to time scrambled recordings of the same story (17 participants in the paragraph-scrambled condition
209 listened to the paragraphs in a randomized order and 36 in the word-scrambled condition listened to
210 the words in a randomized order), or lay resting with their eyes open in the scanner (rest condition; 36
211 participants). We sought to demonstrate how higher-order correlations may be used to examine dynamic
212 interactions of brain patterns in (real) multi-subject fMRI datasets. This story listening dataset was col-
213 lected as part of a separate study, where the full imaging parameters, image preprocessing methods, and
214 experimental details may be found (Simony et al., 2016). The dataset is available at <http://arks.princeton.edu/ark:/88435/dsp015d86p269k>. Bars of each color display cross-validated decoding performance for
216 decoders trained using different sets of neural features: whole-brain patterns of voxel activities

217 We next evaluated if our model of high-order correlations in brain activity can capture cognitively
218 relevant brain patterns. We performed a decoding analysis, using cross validation to estimate (using other
219 participants' data) which parts of the story each weighted-mixture of higher-order brain activity pattern
220 corresponded to (see *Materials and methods*). We note that our primary goal was not to achieve perfect
221 decoding accuracy, but rather to use decoding accuracy as a benchmark for assessing whether different
222 neural features specifically capture cognitively relevant brain patterns.

223 Separately for each experimental condition, we divided participants into two groups. For the zeroth
224 order, we computed the mean factor activity for each group. For all subsequent orders up to the tenth
225 order, we computed the mean approximated dynamic ISFC of factor activity for each group (see *Materials*
226 and *methods*), and combined in a weighted mixutre with all previous orders (i.e. cross-validation for the
227 second order contained a weighted-mixture of zeroth, first, and second order (Fig. 4, c. and f.). For each
228 order, we correlated the group 1 activity patterns with group 2 activity patterns. We then subdivided
229 the group 1 to obtain an optimal weighting parameter for each order's correlation matrix using the same
230 cross validation method. We used the optimal weighting parameters to obtain a weighted-mixture (see
231 *Materials and methods*) of each order's correlation matrix. Using these correlations, we labeled the group 1
232 timepoints using the group 2 timepoints with which they were most highly correlated; we then computed
233 the proportion of correctly labeled group 1 timepoints. (We also performed the symmetric analysis whereby

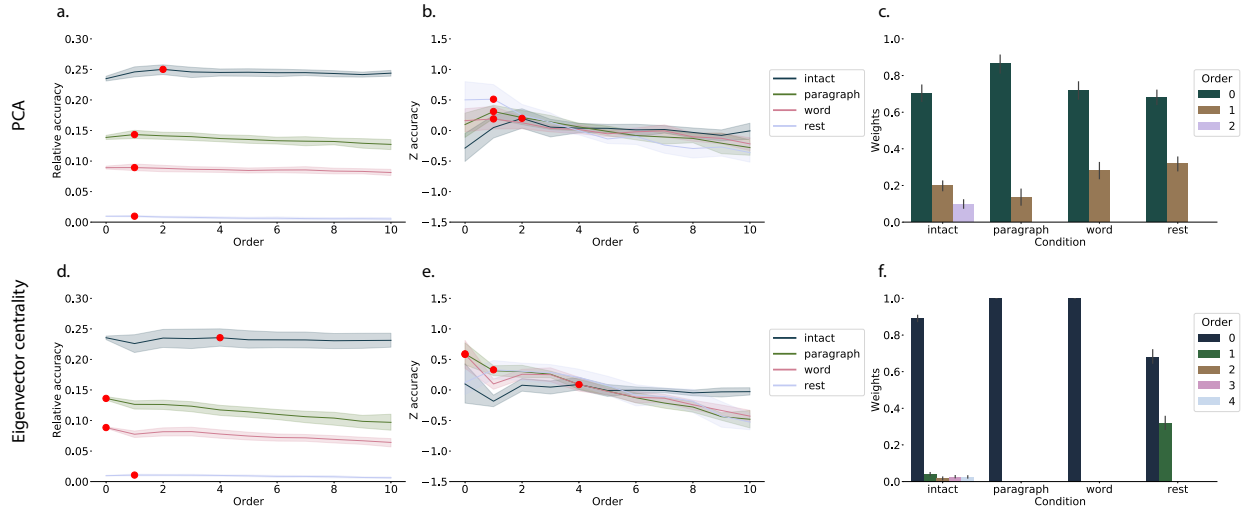


Figure 4: Decoding by order. **a. d. Relative decoding accuracy by order.** Ribbons of each color display cross-validated decoding performance averaged over all parameters for each condition (intact, paragraph, word, and rest) using PCA (a.) or eigenvector centrality (d.) to approximate correlations. Decoders were trained using increasingly more higher-order information and this ribbon are displayed relative to chance at 0. The red dots indicates maximum decoding accuracy for each condition. **b. e. Z-transformed decoding accuracy by order.** We Z-transformed the decoding accuracy by order to better visualize the order with the maximum decoding accuracy for each condition using PCA (b.) or eigenvector centrality (e.) to approximate correlations. **c. f. Optimized weights.** Bar heights indicate the optimized mixing parameter ϕ of each contributing order up to and including the order with the maximum decoding accuracy for each contributing order using PCA (c.) or eigenvector centrality (f.) to approximate correlations. For the order with maximum decoding accuracy by condition, we show barplots of the optimized weights ϕ for each contributing order.

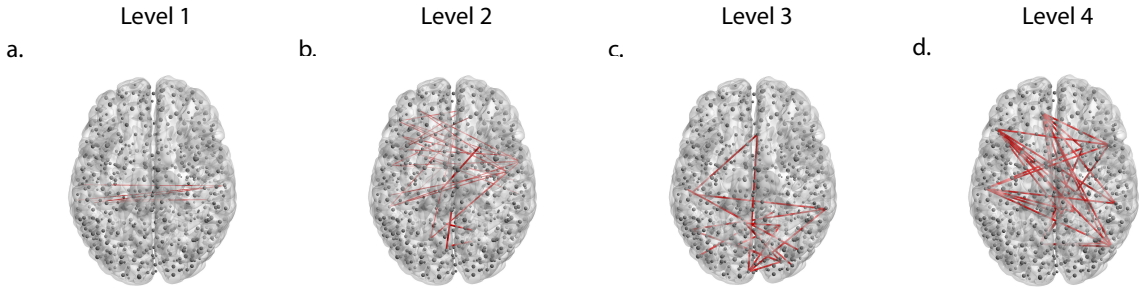


Figure 5: Average correlations by order for the intact listening condition. Using eigenvector centrality to approximate higher-order correlations for the intact listening condition, we plot the strongest 25% absolute value mean correlation for **a. order 1.** **b. order 2.** **c. order 3., and d. order 4.**

we labeled the group 2 timepoints using the group 1 timepoints as a template.) We repeated this procedure 100 times (randomly re-assigning participants to the two groups each time) to obtain a distribution of decoding accuracies for each experimental condition. There were 272 timepoints for paragraph condition, 300 timepoints for intact and word conditions, and 400 timepoints for rest condition, so chance performance on this decoding test is was $\frac{1}{272}$, $\frac{1}{300}$, and $\frac{1}{400}$ respectively.

We repeated this process for each set of parameters, varying kernel type and width, and averaged over the reduction technique used to approximate the higher-order correlations (PCA Fig. 4, a.-c. and eigenvector centrality Fig. 4, d.-f.). Since there is no ground truth in these analyses, and we did not know which parameters best capture the data, we instead report a robustness search by averaging over the parameters and reporting which results consistently showed up across all parameters.

The two methods used to approximate the higher-order correlations (PCA Fig. 4, a.-c. and eigenvector centrality Fig. 4, d.-f.) capture different facets of the activity patterns. Using PCA, the higher-order correlations are all linked to the original activity patterns, whereas eigenvector centrality breaks the immediate link with specific brain areas and instead characterizes the position of the nodes in the network that are similar over time.

We found for both PCA and eigenvector centrality, during the intact condition in the experiment, classifiers that incorporated higher-order correlations yielded consistently higher accuracy than classifiers trained only on lower-order patterns (Fig. 4, a. d.). We plot the average correlations for up to the fourth order for the intact condition Fig. ???. By contrast, we found that incorporating higher-order (greater than first order) correlations did not further improve decoding accuracy for the other listening conditions or rest condition. This suggests that the cognitive processing that supported the most cognitively rich condition involved higher-order network dynamics.

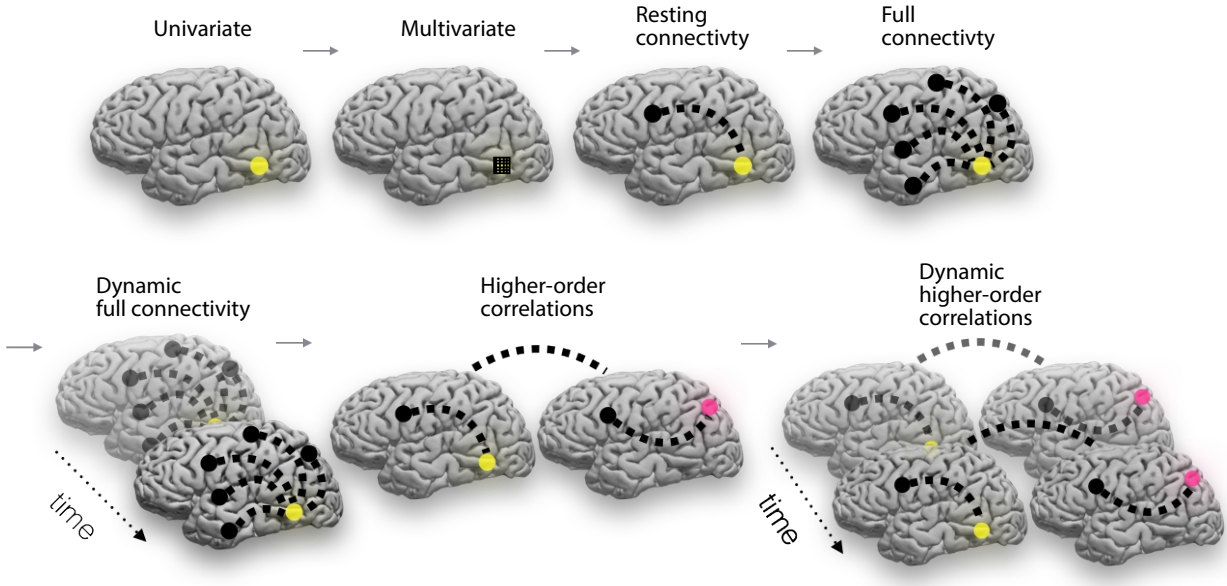


Figure 6: **Direction of the field adapted from (Turk-Browne, 2013).** The evolution of fMRI analyses started with univariate activation, which refers to the average amplitude of BOLD activity evoked by events of an experimental condition. Next, multivariate classifiers are trained on patterns of activation across voxels to decode distributed representations for specific events. The next, resting connectivity, is the temporal correlation of one or more seed regions with the remainder of the brain during rest. Additionally, task-based connectivity examines how these correlations differ by cognitive state. Following this increasing trajectory of increasing complexity, full connectivity considers all pairwise correlations in the brain, most commonly at rest. Next, dynamic full connectivity considers how full connectivity changes over time. Continuing this line of reasoning, we expect higher-order network dynamics might provide even richer insights into the neural basis of cognition.

256 Discussion

257 Based on prior work (CITE) and following the direction of the field (Turk-Browne, 2013) we think our
 258 thoughts might be encoded in dynamic network patterns, and possibly higher order network patterns
 259 (Fig. 5). We sought to test this hypothesis by developing an approach to inferring high-order network
 260 dynamics from timeseries data.

261 One challenge in studying dynamic interactions is the computational resources required to calculate
 262 higher-order correlations. We developed a computationally tractable model of network dynamics (Fig. 2)
 263 that takes in a feature timeseries and outputs approximated first-order dynamics (i.e., dynamic functional
 264 correlations), second-order dynamics (reflecting homologous networks that dynamically form and disperse),
 265 and higher-order network dynamics (up to tenth-order dynamic correlations).

266 We first validated our model using synthetic data, and explored how recovery varied with different
 267 underlying data structures and kernels. We then applied the approach to an fMRI dataset (Simony et al.,
 268 2016) in which participants listened to an audio recording of a story, as well as scrambled versions of the

269 same story (where the scrambling was applied at different temporal scales). We trained classifiers to take
270 the output of the model and decode the timepoint in the story (or scrambled story) that the participants
271 were listening to. We found that, during the intact listening condition in the experiment, classifiers that
272 incorporated higher-order correlations yielded consistently higher accuracy than classifiers trained only
273 on lower-order patterns (Fig. 4, a. d.). By contrast, these higher-order correlations were not necessary
274 to support decoding the other listening conditions and (minimally above chance) during a control rest
275 condition. This suggests that the cognitive processing that supported the most cognitively rich listening
276 conditions involved second-order (or higher) network dynamics.

277 Although we found decoding accuracy was best when incorporating higher-order network dynamics
278 for all but rest condition, it is unclear if this is a product of the brain or the data collection technique . It could
279 be that the brain is second-order or it could be that fMRI can only reliably give second-order interactions.
280 Exploring this method with other data collection technique will be important to disentangle this question.

281 **Concluding remarks**

282 How can we better understand how brain patterns change over time? How can we quantify the potential
283 network dynamics that might be driving these changes? One way to judge the techniques of the future is
284 to look at the trajectory of the fMRI field so far has taken so far (Fig. 2). The field started with univariate
285 activation, measuring the average activity for each voxel. Analyses of multivariate activation followed,
286 looking at spatial patterns of activity over voxels. Next, correlations of activity were explored, first with
287 measures like resting connectivity that take temporal correlation between a seed voxel and all other voxels
288 then with full connectivity that measure all pairwise correlations. Additionally, this path of increasing
289 complexity also moved from static to dynamic measurements. One logical next step in this trajectory would
290 be dynamic higher-order correlations. We have created a method to support these calculations by scalably
291 approximating dynamic higher-order correlations.

292 **Acknowledgements**

293 We acknowledge discussions with Luke Chang, Hany Farid, Paxton Fitzpatrick, Andrew Heusser, Eshin
294 Jolly, Qiang Liu, Matthijs van der Meer, Judith Mildner, Gina Notaro, Stephen Satterthwaite, Emily Whitaker,
295 Weizhen Xie, and Kirsten Ziman. Our work was supported in part by NSF EPSCoR Award Number 1632738
296 to J.R.M. and by a sub-award of DARPA RAM Cooperative Agreement N66001-14-2-4-032 to J.R.M. The
297 content is solely the responsibility of the authors and does not necessarily represent the official views of our

298 supporting organizations.

299 Author contributions

300 Concept: J.R.M. Implementation: T.H.C., L.L.W.O., and J.R.M. Analyses: L.L.W.O and J.R.M.

301 References

- 302 Alvarez-Hamelin, I., Dall'Asta, L., Barrat, A., & Vespignani, A. (2005). *k*-corr decomposition: a tool for the
303 visualization of large scale networks. *arXiv*, cs/0504107v2.
- 304 Barthélemy, M. (2004). Betweenness centrality in large complex networks. *European Physical Journal B*, 38,
305 163–168.
- 306 Bonacich, P. (2007). Some unique properties of eigenvector centrality. *Social Networks*, 29(4), 555–564.
- 307 Christakis, N. A., & Fowler, J. H. (2010). Social network sensors for early detection of contagious outbreaks.
308 *PLoS One*, 5(9), e12948.
- 309 Comon, P., Jutten, C., & Herault, J. (1991). Blind separation of sources, part II: Problems statement. *Signal
310 Processing*, 24(1), 11 - 20.
- 311 Estrada, E., & Rodríguez-Velázquez, J. A. (2005). Subgraph centrality in complex networks. *Physical Review
312 E*, 71(5), 056103.
- 313 Freeman, L. C. (1977). A set of measures of centrality based on betweenness. *Sociometry*, 40(1), 35–41.
- 314 Geisberger, R., Sanders, P., & Schultes, D. (2008). Better approximation of betweenness centrality. *Proceedings
315 of the meeting on Algorithm Engineering and Experiments*, 90–100.
- 316 Gershman, S., Blei, D., Pereira, F., & Norman, K. (2011). A topographic latent source model for fMRI data.
317 *NeuroImage*, 57, 89–100.
- 318 Halu, A., Mondragón, R. J., Panzarasa, P., & Bianconi, G. (2013). Multiplex PageRank. *PLoS One*, 8(10),
319 e78293.
- 320 Hinton, G. E., & Salakhutdinov, R. R. (2006). Reducing the dimensionality of data with neural networks.
321 *Science*, 313(5786), 504–507.

- 322 Honey, C. J., Kötter, R., Breakspear, M., & Sporns, O. (2007). Network structure of cerebral cortex shapes
323 functional connectivity on multiple time scales. *Proceedings of the National Academy of Science USA*, 104(24),
324 10240–10245.
- 325 Jutten, C., & Herault, J. (1991). Blind separation of sources, part I: An adaptive algorithm based on
326 neuromimetic architecture. *Signal Processing*, 24(1), 1–10.
- 327 Lee, D. D., & Seung, H. S. (1999). Learning the parts of objects by non-negative matrix factorization. *Nature*,
328 401, 788–791.
- 329 Lin, J. (2009). Divergence measures based on the Shannon entropy. *IEEE Transactions on Information Theory*,
330 55(1), 145–151.
- 331 Lohmann, G., Margulies, D. S., Horstmann, A., Pleger, B., Lepsien, J., Goldhahn, D., … Turner, R. (2010).
332 Eigenvector centrality mapping for analyzing connectivity patterns in fMRI data of the human brain.
333 *PLoS One*, 5(4), e10232.
- 334 Mairal, J., Ponce, J., Sapiro, G., Zisserman, A., & Bach, F. R. (2009). Supervised dictionary learning. *Advances
335 in Neural Information Processing Systems*, 1033–1040.
- 336 Mairal, J. B., Bach, F., Ponce, J., & Sapiro, G. (2009). Online dictionary learning for sparse coding. *Proceedings
337 of the 26th annual international conference on machine learning*, 689–696.
- 338 Manning, J. R., Ranganath, R., Norman, K. A., & Blei, D. M. (2014). Topographic factor analysis: a Bayesian
339 model for inferring brain networks from neural data. *PLoS One*, 9(5), e94914.
- 340 Manning, J. R., Zhu, X., Willke, T. L., Ranganath, R., Stachenfeld, K., Hasson, U., … Norman, K. A. (2018).
341 A probabilistic approach to discovering dynamic full-brain functional connectivity patterns. *NeuroImage*,
342 180, 243–252.
- 343 McInnes, L., & Healy, J. (2018). UMAP: Uniform manifold approximation and projection for dimension
344 reduction. *arXiv*, 1802(03426).
- 345 Newman, M. E. J. (2005). A measure of betweenness centrality based on random walks. *Social Networks*, 27,
346 39–54.
- 347 Newman, M. E. J. (2008). The mathematics of networks. *The New Palgrave Encyclopedia of Economics*, 2, 1–12.
- 348 Opsahl, T., Agneessens, F., & Skvoretz, J. (2010). Node centrality in weighted networks: generalizing degree
349 and shortest paths. *Social Networks*, 32, 245–251.

- 350 Pearson, K. (1901). On lines and planes of closest fit to systems of points in space. *The London, Edinburgh,
351 and Dublin Philosophical Magazine and Journal of Science*, 2, 559-572.
- 352 Rao, C. R. (1982). Diversity and dissimilarity coefficients: a unified approach. *Theoretical Population Biology*,
353 21(1), 24–43.
- 354 Ricotta, C., & Szeidl, L. (2006). Towards a unifying approach to diversity measures: Bridging the gap
355 between the Shannon entropy and Rao's quadratic index. *Theoretical Population Biology*, 70(3), 237–243.
- 356 Rubinov, M., & Sporns, O. (2010). Complex network measures of brain connectivity: uses and interpreta-
357 tions. *NeuroImage*, 52, 1059–1069.
- 358 Schreiber, T. (2000). Measuring information transfer. *Physical Review Letters*, 85(2), 461–464.
- 359 Simony, E., Honey, C. J., Chen, J., & Hasson, U. (2016). Uncovering stimulus-locked network dynamics
360 during narrative comprehension. *Nature Communications*, 7(12141), 1–13.
- 361 Spearman, C. (1904). General intelligence, objectively determined and measured. *American Journal of
362 Psychology*, 15, 201–292.
- 363 Tipping, M. E., & Bishop, C. M. (1999). Probabilistic principal component analysis. *Journal of Royal Statistical
364 Society, Series B*, 61(3), 611–622.
- 365 Turk-Browne, N. B. (2013). Functional interactions as big data in the human brain. *Science*, 342, 580–584.
- 366 van der Maaten, L. J. P., & Hinton, G. E. (2008). Visualizing high-dimensional data using t-SNE. *Journal of
367 Machine Learning Research*, 9, 2579-2605.
- 368 Zar, J. H. (2010). *Biostatistical analysis*. Prentice-Hall/Pearson.